

# JGR Space Physics

## RESEARCH ARTICLE

10.1029/2019JA026771

### Key Points:

- At  $L = 5$ , 53% of the CIR storms and 30% of the CME storms show electron flux increase
- Relativistic electron flux variations at  $L = 5$  is largely independent of geomagnetic storm strength but strongly depends upon averaged  $V_{sw}$  and IMF  $B_z$
- At  $L = 3$ , >71% geomagnetic storms show no remarkable electron flux variations, irrespective of the storm driver

### Correspondence to:

B. Veenadhari,  
veenaiig@gmail.com

### Citation:

Pandya, M., Veenadhari, B., Ebihara, Y., Kanekal, S. G., & Baker, D. N. (2019). Variation of radiation belt electron flux during CME- and CIR-driven geomagnetic storms: Van Allen Probes observations. *Journal of Geophysical Research: Space Physics*, 124. <https://doi.org/10.1029/2019JA026771>

Received 28 MAR 2019

Accepted 28 JUN 2019

Accepted article online 12 JUL 2019

## Variation of Radiation Belt Electron Flux During CME- and CIR-Driven Geomagnetic Storms: Van Allen Probes Observations

Megha Pandya<sup>1</sup> , Veenadhari Bhaskara<sup>1</sup> , Yusuke Ebihara<sup>2</sup> , Shrikanth G. Kanekal<sup>3</sup> , and Daniel N. Baker<sup>4</sup> 

<sup>1</sup>Indian Institute of Geomagnetism, Navi Mumbai, India, <sup>2</sup>Research Institute for Sustainable Humanosphere, Kyoto University, Uji, Japan, <sup>3</sup>NASA Goddard Space Flight Center, Greenbelt, MD, USA, <sup>4</sup>Laboratory for Atmospheric and Space Physics, Boulder, CO, USA

**Abstract** Relativistic electron flux responses in the inner magnetosphere are investigated for 28 magnetic storms driven by corotating interaction region (CIR) and 27 magnetic storms driven by coronal mass ejection (CME), using data from the Relativistic Electron-Proton Telescope instrument on board Van Allen Probes from October 2012 to May 2017. In this present study we analyze the role of CIRs and CMEs in electron dynamics by sorting the electron fluxes in terms of averaged solar wind parameters,  $L$ -values, and energies. The major outcomes from our study are the following: (i) At  $L = 3$  and  $E = 3.4$  MeV, for >70% cases the electron flux remains stable, while at  $L = 5$ , for ~82% cases it changes with the geomagnetic conditions. (ii) At  $L = 5$ , ~53% of the CIR storms and 30% of the CME storms show electron flux increase. (iii) At a given  $L$ -value, the tendency for the electron flux variation diminishes with the increasing energies for both categories of storms. (iv) In case of CIR-driven storms, the electron flux changes are associated with changes in  $V_{sw}$  and  $Sym-H$ . (v) At  $L \sim 3$ , CME storms show increased electron flux, while at  $L \sim 5$ , CIR storms are responsible for the electron flux enhancements. (vi) During CME- and CIR-driven storms, distinct electron flux variations are observed at  $L = 3$  and  $L = 5$ .

## 1. Introduction

Geomagnetic storms can drastically affect the charged particles population trapped in the Earth's Van Allen radiation belt (e.g., Baker & Kanekal, 2008; Kanekal, 2006; McIlwain, 1966). It is now well established that the electron flux decreases during the geomagnetic storm main phase and often recovers back after the storm has passed [Friedel et al., 2002; Kim & Chan, 1997; Miyoshi et al., 2003; Nakamura et al., 1998; Soraas & Davis, 1968]. However, the temporal and spatial growth of radiation belt electrons can vary from storm to storm. Reeves et al. (2003) studied the response of electron flux at  $L = 3$ –8 and found that only about 50% of all storms resulted in increased fluxes, whereas 25% shows decreased fluxes and 25% shows little to no change. It is currently believed that this is due to a balance between energization and loss processes, with net flux being the result of their relative strengths.

Relativistic electrons also respond to the impact of an interplanetary (IP) shock on the Earth's magnetosphere (Blake et al., 1992; Kanekal et al., 2016; Li et al., 1993). For the extreme event in March 1991, Li et al. (1993) simulated the response of relativistic electron flux to the IP shock and showed that the injection and energization resulted from a nonresonant interaction of the particles with the time-varying electric field induced by the shock. Zong et al. (2009, 2017) studied relationship between the energetic electron bursts and the large shock-induced ultralow frequency (ULF) waves. They found that energetic electrons can be accelerated efficiently by poloidal mode ULF waves that have a sufficiently strong electric field in the direction of electron drift motion. Moreover, IP shocks with even a small change in dynamic pressure can have a non-negligible role in the radiation belt dynamics (Zong et al., 2009). Recently, Hao et al. (2019) demonstrated that the acceleration of ultrarelativistic electrons (up to 3.4 MeV) in the outer radiation belt is due to drift resonance by poloidal ULF waves.

Paulikas and Blake (1979) and Baker et al. (1979) found that average electron flux varies concurrently with the solar wind velocity. High-speed solar wind streams do not always result in large flux enhancement (Kim et al., 2006; Li et al., 2011; Reeves et al., 2011) and southward interplanetary magnetic field (IMF)  $B_z$  is a second major factor (apart from elevated solar wind speed) necessary for electron flux

enhancements (Blake et al., 1997; Li et al., 2005). When IMF  $B_z$  is southward, frequent substorms are expected. These substorms provide a seed population (Baker et al., 1998), which are energized by the plasma waves produced by anisotropy of lower energy source population (Jaynes et al., 2015). Frequently injected hot electrons give rise to the excitation of the whistler mode chorus waves that accelerate electrons by way of resonant interaction (Li et al., 2005; Miyoshi et al., 2013). Recently, Li et al. (2015) found that the prolonged southward IMF  $B_z$ , high solar wind velocity, and low solar wind dynamic pressure are critical factors for the efficient megaelectron volt electron acceleration, especially when all the three conditions are operating simultaneously. Moreover, the presence of source and seed population is also crucial.

Many statistical studies have also been dedicated to the understanding of role of solar wind parameters to the changing radiation belt electron flux during a magnetic storm. For 33 magnetic storms that resulted in enhanced electron flux and 29 storms that did not, O'Brien et al. (2001) conducted a cross-correlation analysis for solar wind and geomagnetic activity data for outer radiation belt electrons at geosynchronous orbit for 0.3–1.5 and >2-MeV energies. They found that the sustained solar wind velocity >450 km/s and long-duration elevated Pc5 ULF wave power during the recovery phase are the best indicators to describe the storms giving electron flux enhancements. Anderson et al. (2015) used LANL 1.8- to 3.5-MeV electron flux data and studied 342 magnetic storms with  $Dst > -50$  nT. They found that these storms are less (more) likely for the electron flux enhancement (depletion) at geosynchronous orbit. Recently, some studies are dedicated to electron flux variations using National Aeronautics and Space Administration's Van Allen Probes [Baker et al., 2014; Kilpua et al., 2015; Li et al., 2015; Shprits et al., 2017; Turner et al., 2015, 2016; Zhao et al., 2017]; however, the causes for the different response of the electron flux are still unclear.

The response of the outer zone electron flux is also dependent on the solar wind driver of magnetic storms, coronal mass ejections (CMEs), and corotating interaction regions (CIRs; e.g., Borovsky & Denton, 2006; Denton et al., 2006; Kataoka & Miyoshi, 2006; Yuan & Zong, 2012) as well as more complex driver conditions (Kanekal et al., 2015). The electron flux variations are strongly governed by substructures of the solar wind storm drivers (sheath, ejecta, and interface region) and prestorm electron flux levels (Hietala et al., 2014; Kilpua et al., 2015). CME sheath-driven storms are highly effective for electron losses due to outward radial diffusion and magnetopause shadowing. The mechanisms responsible for the development of radiation belt electrons during CME- and CIR-driven geomagnetic storms are likely to differ and depend upon the various parameters including IMF (Denton et al., 2006; Miyoshi et al., 2007 and Shen et al., 2017). Turner et al. (2015) studied the response of 52 geomagnetic storms in the energy range of tens of kiloelectron volts to 2 MeV and showed that at a given  $L$ -shell the peak electron flux correlates to the geomagnetic storm magnitude only. Very recently, Turner et al. (2019) investigated a detailed statistical study of electron radiation belt response to the geomagnetic storms as a function of energy and  $L$ -shell for 30 keV to 6.3 MeV by considering the storms driven by CME shocks/sheaths and ejecta and found depletion of >1 MeV for outer belt and an enhancement of megaelectron volt electrons at lower  $L$ -shells. The energization or loss of radiation belt electrons are not completely understood with the existing theories of adiabatic changes observed to occur during gradual buildup of the ring current (Kim & Chan, 1997) and magnetopause shadowing (Kang et al., 2018; Shprits et al., 2006; Wilken et al., 1986). So more interesting future studies can be carried out by selecting different solar drivers and solar wind parameters for each  $L$ -shell indicating inner and outer belt variations as mentioned by Turner et al. (2019).

This present work is based upon statistical analysis of different geomagnetic storm drivers and IP parameters on relativistic electron flux variations using data from the Relativistic Electron-Proton Telescope (REPT) instrument for 28 magnetic storms driven by CIR and 27 magnetic storms driven by CME, for the period of October 2012 to May 2017. Here, we continue to develop and extend previous studies of the electron flux response by not only focusing on different energies but also different  $L$ -values (e.g., Turner et al., 2019). We subcategorize the solar wind driving conditions based on magnitude of IMF  $B_z$ ,  $V_{sw}$ , and  $P_{sw}$ . We also refined the previous studies by clearly separating the storm driver, that is, CME- and CIR-driven magnetic storms. The paper is organized as follows. Section 2 deals with the description of the satellite data and selection of events in our study. Section 3 gives the observation and results of electron flux variations at different  $L$ -range and energies. In section 4, we discuss our results followed by a summary in section 5.

## 2. Data

For the present study, we used the data from the REPT (Baker et al., 2012) instrument on board Van Allen Probes. The Van Allen Probes mission comprises of identically instrumented twin spacecraft flying in a highly elliptical, low inclination orbit ( $1.1 \times 5.8 R_E$ , inclination of  $\sim 10^\circ$ , orbital period of  $\sim 9$  hr) since August 2012 (Mauk et al., 2014). In the  $L \leq 2$  region, the electron channels are contaminated due to the presence of background from inner zone penetrating protons. This makes electron flux measurements uncertain and hence we studied the electron flux above  $L = 3$ . REPT instrument resolves the electron flux into 12 different energy channels from 1.8 to 20 MeV.

Our study uses 1-min resolved symmetric component of the ring current (*Sym-H*), which is a high-resolution version of the hourly *Dst* index (Wanliss & Showalter, 2006). The IP solar wind plasma parameters at the Earth's orbit are from the OMNI database (King & Papitashvili, 2005) and solar wind data are from Advanced Composition Explorer, Wind, IMP 8, and Geotail spacecraft measurements. We investigate the variation of relativistic electron flux with the geomagnetic activity from October 2012 to May 2017. We select geomagnetic storms based on minimum *Sym-H* being less than  $-50$  nT and classified into two types in terms of minimum *Sym-H*. The geomagnetic storms with  $-90$  nT < minimum *Sym-H* <  $-50$  nT are considered as moderate, while the ones with minimum *Sym-H* <  $-90$  nT are considered as intense. The geomagnetic storms are further classified based on their solar drivers, namely, CME and CIR. Table 1 differentiates the geomagnetic storms according to their solar wind drivers such as CMEs and CIRs. The CME storms are induced by a shock and has a sudden increase in IMF  $B_z$ ,  $V_{sw}$ , and proton density (Marcia & Raymond, 1997), while the CIR-driven magnetic storms can be identified with enhanced solar wind flow speed, decreased proton density and fluctuating IMF  $B_z$ . The list so obtained is then verified with Shen et al. (2017). Upon classifying these geomagnetic storms, we obtain 27 CME-driven and 28 CIR-driven geomagnetic storms. We calculated the electron flux for inbound and outbound passages separately and hence we have 110 observations corresponding to 55 geomagnetic storms.

Figures 1a and 1b show an example of the radiation belt electron flux variation for CIR- and CME-driven geomagnetic storms. *Sym-H*, IMF  $B_z$ , solar wind dynamic pressure ( $P_{sw}$ ), and solar wind velocity ( $V_{sw}$ ) are shown in lower panels of Figure 1 for each geomagnetic storm. The minimum *Sym-H* values are almost same. The top most panel of Figure 1 shows a spectrogram of spin-averaged differential electron flux of relativistic electron flux in the range of 1–20 MeV, color coded according to the bar to the right. It is seen that the electron flux depletes during the geomagnetic main phase for the CIR-driven and CME-driven storms and recovers promptly and exceeds the prestorm level for the CIR-driven storm. As for the CME-driven storm, the electron flux recovers gradually.

In the following sections, we carry out a detailed analysis to study the interesting behavior of radiation belt electrons for CME- and CIR-driven geomagnetic storms that occurred during the period from October 2012 to May 2017.

## 3. Observation and Results

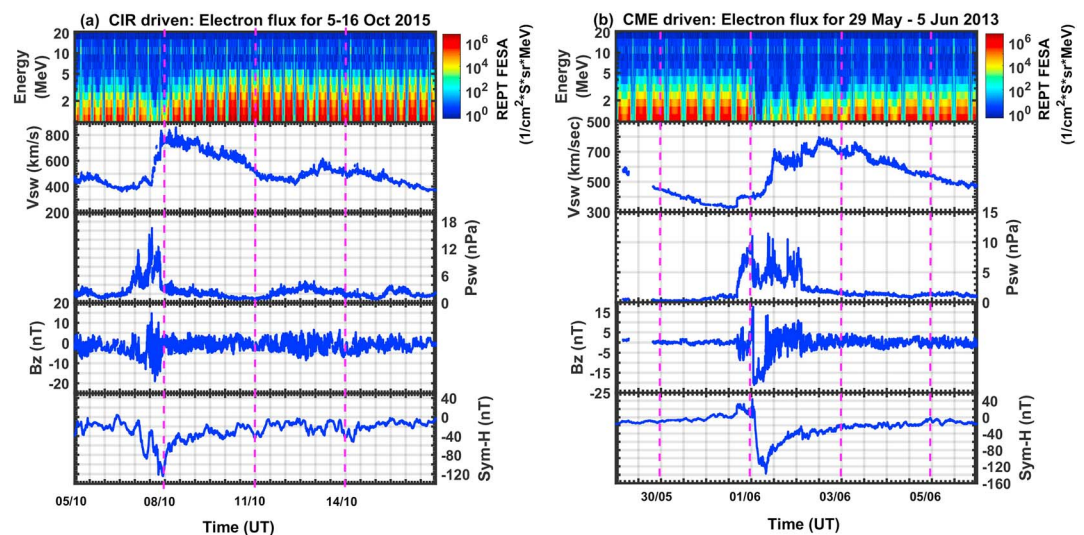
### 3.1. Relativistic Electron Flux Variation With Different Storm Drivers

Figure 2 shows relativistic electron fluxes (3.4–5.2 MeV) measured by Probe-A as a function of  $L$ -shell and time for three CME-driven geomagnetic storms. We selected these three CME-driven geomagnetic storms as an example illustrating relativistic electron flux variations such that they flux show (a) an enhancement, (b) a depletion, and (c) almost no change, respectively. The lower most panel in Figure 2 shows the *Dst* index, reflecting the strength of the storm time ring current as well as all the other magnetospheric current. The duration starting from the time the *Dst* index begins to decrease after sudden commencement ( $t_0$ ) until the *Dst* minimum ( $t_1$ ) is referred to as “at-storm” interval, covering the main phase of the storm. For the geomagnetic storms that do not have sudden commencement (especially for CIR storms), the at-storm interval is considered when *Dst* begins to decrease ( $t_0$ ) monotonically until the *Dst* minimum ( $t_1$ ). So the at-storm interval is from  $t_0$  to  $t_1$ . We also define “prestorm flux” as the maximum flux in the prestorm interval that ranges from  $t_0-1$  to  $t_0-4$  days. We define “poststorm flux” is the maximum flux in the poststorm interval that ranges from  $t_1+1$  to  $t_1+6$  days. These are shown as yellow-shaded portions in each lower panel in Figure 2. The maximum electron flux variation in each

**Table 1**  
List of CME and CIR driven magnetic storms

Sr. no	CME-driven storms	Sym-H (nT)	CIR-driven storms	Sym-H (nT)
1	2012-10-01/03:52	-138	2013-01-26/22:19	-62
2	2012-10-09/02:10	-116	2013-03-01/10:12	-76
3	2012-11-14/07:27	-118	2013-03-29/16:17	-64
4	2013-03-17/20:28	-132	2013-08-27/21:43	-64
5	2013-06-01/07:48	-137	2013-10-30/23:20	-57
6	2013-06-29/06:36	-111	2013-12-08/08:30	-72
7	2013-07-06/08:33	-80	2014-06-08/06:50	-72
8	2013-10-02/06:19	-90	2015-02-17/23:55	-70
9	2014-02-19/08:23	-127	2015-02-24/03:36	-76
10	2014-02-27/23:24	-101	2015-03-02/08:51	-70
11	2014-04-12/08:32	-92	2015-04-16/23:29	-88
12	2014-04-30/09:10	-76	2015-05-13/06:59	-98
13	2014-08-27/18:18	-90	2015-06-08/07:45	-105
14	2014-09-12/23:03	-97	2015-07-05/04:52	-58
15	2014-12-22/05:25	-65	2015-07-13/10:54	-71
16	2015-01-07/11:00	-135	2015-10-07/22:23	-124
17	2015-03-17/22:47	-234	2016-01-20/16:42	-95
18	2015-06-23/04:24	-208	2016-02-03/02:52	-60
19	2015-07-23/07:28	-83	2016-02-18/00:28	-60
20	2015-08-16/07:37	-94	2016-03-06/21:20	-110
21	2015-08-27/20:32	-101	2016-05-08/08:15	-105
22	2015-09-09/08:03	-113	2016-07-25/17:17	-51
23	2015-11-07/06:05	-106	2016-08-03/06:49	-63
24	2015-12-20/22:49	-170	2016-08-23/21:13	-83
25	2015-12-31/23:56	-99	2016-09-02/01:53	-74
26	2016-03-06/21:20	-110	2016-09-29/09:32	-64
27	2016-10-13/23:45	-114	2017-03-01/22:17	-74
28			2017-03-27/14:45	-86

Note. Dates are formatted as YYYY-MM-DD. CIR = corotating interaction region; CME = coronal mass ejection.



**Figure 1.** Energy versus time spectra for spin averaged differential electron flux for (a) CIR-driven geomagnetic storm of 5–16 October 2015 and (b) CME-driven geomagnetic storm of 29 May to 5 June 2013 is shown. The lower panels show corresponding solar wind parameters,  $V_{sw}$ ,  $P_{sw}$ , and IMF  $B_z$ . The lower most panel gives the intensity of the geomagnetic storm  $Sym-H$ . CIR = corotating interaction region; CME = coronal mass ejection; REPT = Relativistic Electron-Proton Telescope.

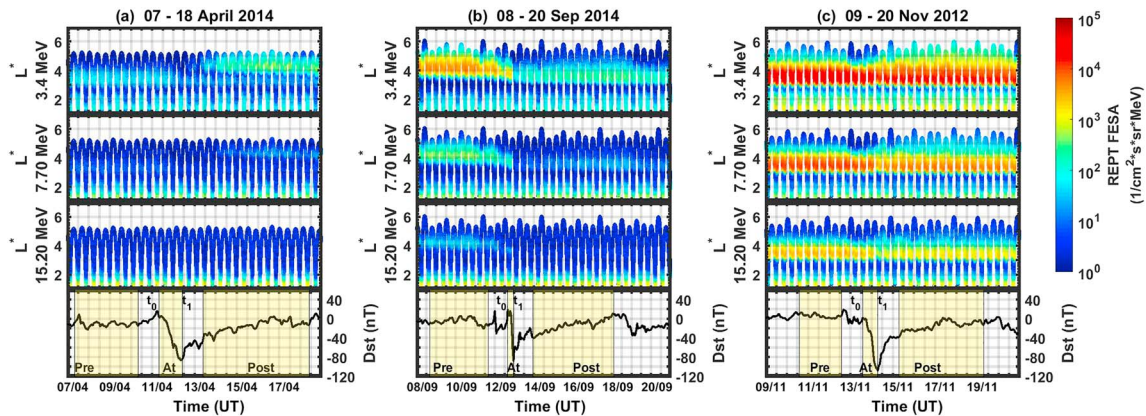


**Figure 2.** L-value versus time spectra of spin averaged differential electron flux at three different energy channels 3.4, 4.2, and 5.2 MeV is shown for coronal mass ejection-driven geomagnetic storms (a) 7–18 April 2014, (b) 8–20 September 2014, and (c) 9–20 November 2012. During the poststorm interval, the electron flux may (a) increase, (b) decrease, and (c) no change in comparison with the prestorm interval. REPT = Relativistic Electron-Proton Telescope.

interval can then be studied for all geomagnetic storms and classified as enhancement, depletion, or no change for a given energy and at each  $L$ -value. With this clear definition, the electron flux variation during a geomagnetic storm may fall into the categories of flux enhancement, depletion and no change for a given  $L$ -value; that is, the same storm might exhibit these characteristics depending upon spatial location ( $L$ -value) of measurement.

Figure 2a shows electron flux variation during a moderate geomagnetic storm of 12 April 2014 with  $Dst$  minimum  $-87$  nT. When the magnetic storm begins, the flux of relativistic electron decreases for all the energy channels at  $L < 4$ . This is immediately followed by a rapid enhancement of the electron flux at higher  $L$ -shells; that is,  $L > 4$ . At  $L = 5$  and  $E = 3.4$  MeV, the electron flux during the poststorm interval increases by a factor of  $\sim 31$  than the prestorm flux. Figure 2b shows electron flux variation during the geomagnetic storm of 12 September 2014, having nearly similar strength of geomagnetic activity ( $Dst = -88$  nT). As it is evident from the figure, the response of the radiation belt electrons is quite different with electron flux decrease during the storm main phase but no subsequent increase of electron flux. At  $L = 5$  and electron energy  $E = 3.4$  MeV, the prestorm flux is greater than poststorm relativistic electron flux by the factor of  $\sim 5,000$ . This flux decrease was observed at  $L > 3$ , suggesting an irreversible loss of particles from the trapping region. Figure 2c shows electron flux variation during the moderately intense geomagnetic storm of 13 November 2012, having a  $Dst$  minimum of  $-108$  nT. The electron flux shows only a slight variation before and after the geomagnetic storm.

Figure 3 shows examples of the radiation belt electrons for CIR-driven geomagnetic storms. We determine  $t_0$  and  $t_1$  in the same manner used for the CME-driven storms. For the magnetic storms having double peak minima of  $Dst$ , we consider at-storm interval only for the lowest minimum  $Dst$  ( $t_1$ ). When the second minimum peak exists near  $t_1$ , we define “prestorm interval” and “poststorm interval” as follows. When  $t_{11}$  exists before  $t_0$ , we define “prestorm” interval as the period from  $t_{11}-1$  to  $t_{11}-4$  days. When  $t_{11}$  exists after  $t_1$ , we define “poststorm” interval as the period from  $t_{11}+1$  to  $t_{11}+6$  days. For the geomagnetic storm of 18 February 2016 (Figure 3a) with minimum  $Dst$  of  $-48$  nT, a significant increase in the electron flux is seen during the recovery phase. At  $L = 5$  and electron energy  $E = 3.4$  MeV, the poststorm flux increased by the factor of  $\sim 3,000$ . The increase is more significant at lower energies (i.e., 3.4 MeV). For the geomagnetic storm of 3 February 2016 (Figure 3b), having minimum  $Dst$  of  $-53$  nT, the electron flux shows a decrease but does not re-buildup during its poststorm interval. At  $L = 5$  and electron energy  $E = 3.4$  MeV, the prestorm flux was almost 8 times the poststorm flux. During the magnetic storm of 8 December 2013 (minimum  $Dst$  of  $-66$  nT), the electron flux does not respond significantly to the magnetic storm and hence remains almost unchanged. The complex response of electron flux variation changes with each phase of the storm at different energies and  $L$ -values for all CIR- and CME-driven geomagnetic storms. Hence, we carried out a detailed analysis of electron flux variations for each CME- and CIR-driven geomagnetic storm during prestorm, at-storm and poststorm intervals is at different  $L$ -values and energies.

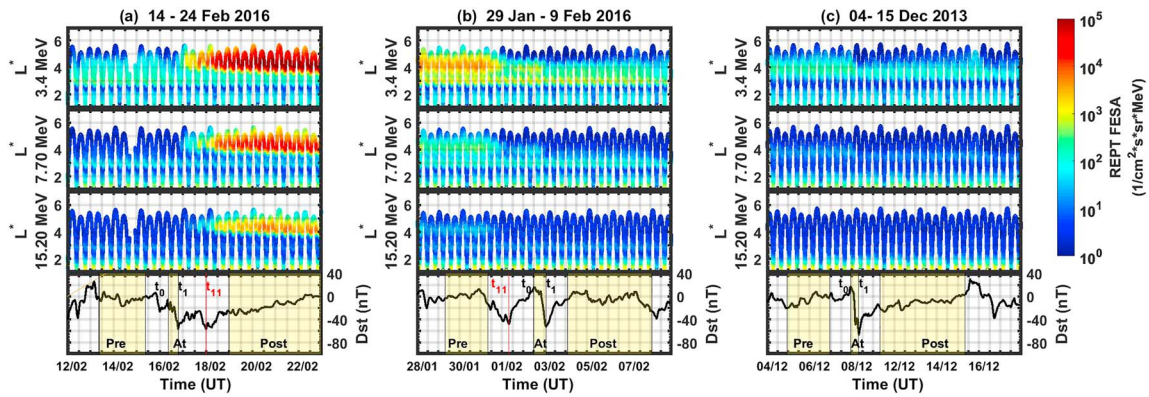


**Figure 3.** Same as Figure 2 except for the corotating interaction region-driven geomagnetic storms.

### 3.2. Relativistic Electron Flux Variation at Different $L$ -Values

We quantitatively examined the variability of relativistic electron fluxes at different  $L$ -shells in response to the 28 CIR- and 27 CME-driven geomagnetic storms. In order to establish clear signatures of maximum flux variations at a given  $L$ -value, we calculate  $j_{\max}(L, K)$ , which is the maximum value of the differential flux averaged over a specified interval (i.e., prestorm, at-storm, or poststorm) at a given  $L$ -value and kinetic energy  $K$  using REPT spin-averaged differential flux. The analysis represented in this work is for  $L = 3$  and 5, and the kinetic energy to be 3.4, 4.2, 5.2, and 7.7 MeV. As Van Allen Probes take measurement at the extreme ends of radiation belts, we show the distinction in the electron flux variation in the inner edge of the outer belt ( $L = 3$ ) and outer edge of outer belt ( $L = 5$ ) with the most dynamic band of energies from 3.4 to 7.7 MeV.

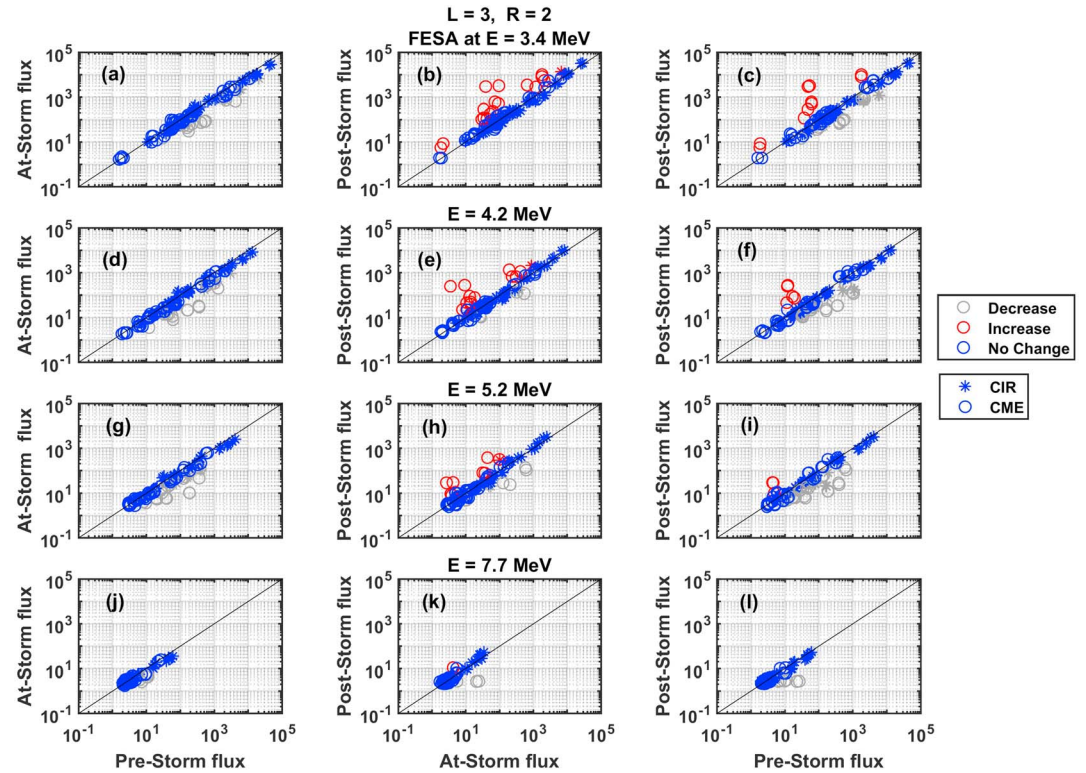
Figure 4 shows the correlation between  $j_{\max}$  values at  $L = 3$  at for electron energies ranging from 3.4 to 7.7 MeV for prestorm and at-storm fluxes (a, d, g, and j), at-storm and poststorm fluxes (b, e, h, and k), and prestorm and poststorm fluxes (c, f, i, and l). Data for CIR-driven geomagnetic storms are represented by the asterisks, while the CME-driven geomagnetic storms are denoted by the open circles. Red (gray) color represent the ratios being increased (decreased) by a factor of 2 or more, while blue color indicates “no change” (absolute value of the ratio is  $<2$ ). Here, the factor “2” is taken as a threshold to distinguish increase/decrease/unchanged. The figure shows that the electron flux tends to decrease during the developing phase (from poststorm to at-storm, a, d, g, and j) and to increase during the declining phase (from at-storm to poststorm, c, f, i, and l) regardless of the storm driver. However, the majority of data points belong to no change during developing and declining phases of the magnetic storm for all the energies. It is important to note that the degree of the response to the magnetic storms is smaller at 7.7 MeV than those at lower energies. In addition, the large changes (indicated by gray and red color) in the flux take place for the CME-driven storms (open circles), irrespective of the strength of magnetic activity.

Figure 5 is the same as Figure 4, except for  $L = 5$ . The electron flux varies drastically in comparison with that at  $L = 3$ . For many geomagnetic storms, the electron flux tends to decrease at all the energy channels during the developing phase (a, d, g, and j), while it tends to increase during the declining phase (b, e, h, and k). Upon comparing with the prestorm flux, the poststorm flux tends to increase largely (c, f, i, and l). For the majority of the cases, the electron flux dynamics is irrespective of the prestorm flux interval. The large increase in the declining phase (b, e, h, and k) is found to occur for the CIR-driven storms. Again, the degree of the change in the fluxes decreases with increasing energy. The flux remains almost steady during each phase of the magnetic storm for 7.7 MeV.

We calculate the ratio defined by the following equation:

$$R(L, K) = \frac{j_{\max}(L, K)|_{\text{poststorm}}}{j_{\max}(L, K)|_{\text{prestorm}}} \quad (1)$$

to quantitatively examine the nature of electron flux variability. Figure 6 shows histograms of the ratios  $R$  for  $L = 3$ . For all the storm drives (both the CME and CIR storms, panels a–d),  $>71\%$  observations show no



**Figure 4.** Statistical results for 3.4- to 7.7-MeV electron flux variation at  $L = 3$  for three intervals at-storm and prestorm (a, d, g, and j; developing phase), poststorm and at-storm (b, e, h, and k; declining phase), and prestorm to declining time (c, f, i, and l). The observations of inbound and outbound passages of the satellite are merged for CME- (circle) and CIR- (asterisk) driven geomagnetic storms. The colors red, gray, and blue stand for increase, decrease, and no change in the flux. CIR = corotating interaction region; CME = coronal mass ejection.

significant change in the electron flux, in particular, at higher energies as shown in Figures 6a–6d. A similar tendency is found for the CIR-driven magnetic storms (panels e–h), and the CME-driven magnetic storms (panels i–l). A noticeable difference between the CIR- and CME-driven storms at  $L = 3$  is that an increase of the electron flux was observed only for the CME-driven storms.

Figure 7 is the same as Figure 6 except that  $L = 5$ . At 3.4 MeV (panel a), the electron flux shows a significant change and 53% of them increase and 30% of them decrease. The drastic variations are reduced for higher energies (panels c and d). Interestingly, the increase cases have a higher ratio in the CIR magnetic storms than in the CME magnetic storms. This tendency is opposite to that found at  $L = 3$ . Though not shown here, the electron flux variations at  $L = 4$  remains in the transitional state between  $L = 3$  and  $L = 5$ . At 3.4 MeV, ~40% of the cases (CME + CIR) shows electron flux increase, while 35% decreased and 25% did not change.

Figure 8 summarizes cumulative distribution functions (CDFs) calculated for the ratio  $R$  at  $L = 3$  (a–d) and  $L = 5$  (e–h). The CDF curves give the probability that a storm has a flux change ratio less than a certain value. These integrated histograms do not suffer from the binning issues and can be easily analyzed by studying the percentage change in the curves. We use Kolmogorov-Smirnov test (Press et al., 2007) to determine the statistical probability that the difference between the distribution is random. The Kolmogorov-Smirnov is defined as the maximum value of the absolute difference between CME- and CIR-driven CDFs. For comparing two different CDFs, namely,  $F_{N1}(x)$  and  $F_{N2}(x)$  having  $N1$  and  $N2$  number of samples, the K-S can be computed using

$$\Delta = \max_{-\infty < x < \infty} |F_{N1}(x) - F_{N2}(x)| * 100 \quad (2)$$

The larger the value of  $\Delta$ , the higher is the confidence for the two distributions to be significantly different. To determine the significance ( $S$ ) of the observed value of  $\Delta$ , we calculate the  $p$  value of the observed nonzero  $\Delta$  as a

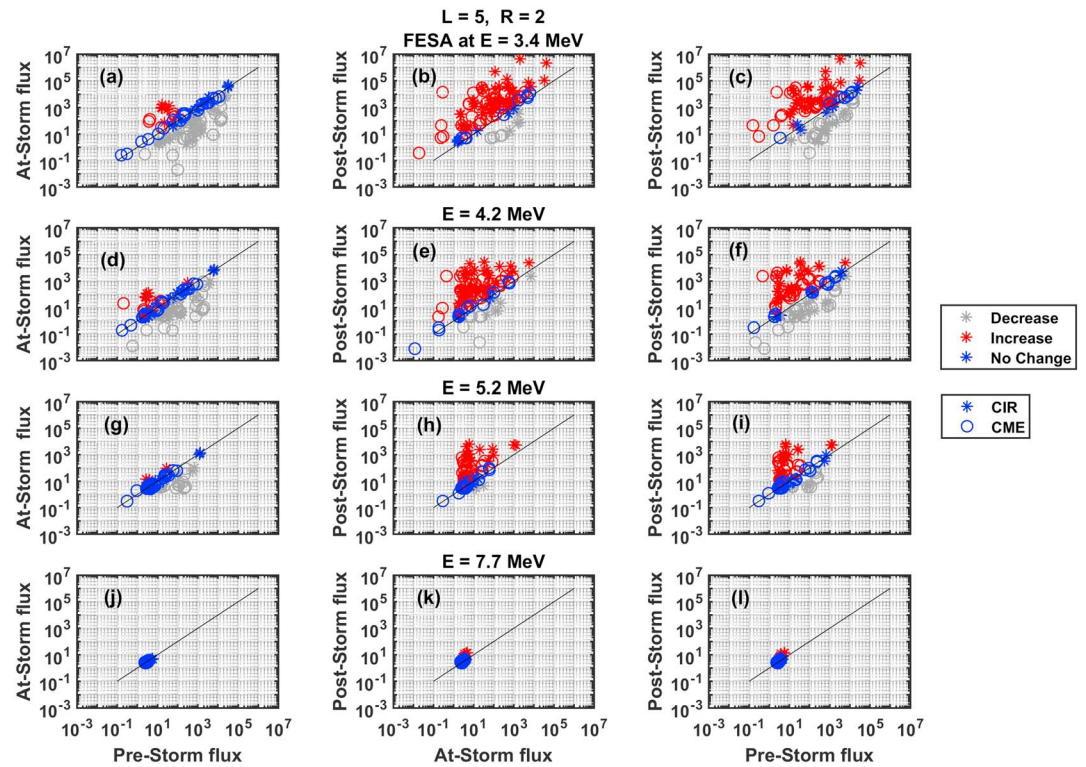


Figure 5. Same as Figure 4 except for  $L = 5$ .

measure of confirmation against the null hypothesis (Press et al., 2007). Hence, the significance “S” define the measure of randomness in the difference. The value of  $S$  is shown by black line in each panel. At  $L = 3$  (panels a–d), the CDF curves are nearly independent of energy at low energies ( $\leq 5.2$  MeV), showing that the CDF curves tend to be shallower for the CME-driven storms than for the CIR-driven storms. At  $L = 5$ , the CDF curves for the CIR-driven storms are shifted toward higher  $R$  values (equation (1)), in comparison with that for the CDF curves for the driven CME storms at low energies ( $\leq 5.2$  MeV). In addition, the curves depend clearly on the energy. At the highest energy (7.7 MeV), no significant difference in the curves are observed because most of the  $R$  values are closed to unity.

### 3.3. Dependence on IMF $B_z$ , Solar Wind Parameters, and $Sym-H$

We further examined the CDF curves for different IMF, solar wind parameters, and  $Sym-H$ , which are shown in Figures 9–12. Figure 9 shown the CDF curves for different IMF  $B_z$  ( $< -5$  and  $> -5$  nT), different solar wind velocity ( $< 500$  and  $> 500$  km/s), different solar wind dynamic pressure ( $< 4$  and  $> 4$  nPa), and different  $Sym-H$  ( $< -100$  and  $> -100$  nT) for the CIR-driven storm. All the parameters, IMF  $B_z$ ,  $V_{sw}$ ,  $P_{sw}$ , and  $Sym-H$ , are averaged over the period between  $t_0$  and  $t_1$ . It is interesting note that the flux variations show a clear dependence on strength of IMF  $B_z$ , and  $Sym-H$  at low energies ( $\leq 5.2$  MeV). This probably indicates that strong southward IMF  $B_z$  tends to give rise to the decrease in the flux. Figure 10 is the same as Figure 9 except at  $L = 5$ . The dependence of the CDF curves on  $V_{sw}$  and  $Sym-H$  is prominent, whereas the dependence on IMF  $B_z$  and  $P_{sw}$  is relatively weak. The dependence is weak for higher energies and almost vanishes at 7.7 MeV. It is noteworthy to understand that these results are drawn according to IMF and solar wind parameters during storm main phase.

Similar analyses of the CDF curves are repeated for the CME-driven storms at  $L = 3$  (Figure 11) and  $L = 5$  (Figure 12). We find that the CDF curves at  $L = 5$  do not show a significant difference between  $L = 3$  and  $L = 5$ , although the dynamic range in the abscissa is different. For the dependence on IMF  $B_z$ , it is clearly seen that the electron flux increases for large southward IMF  $B_z$  ( $B_z < -6$  nT). This is opposite to the tendency for the CIR-driven storms (Figure 10). Electron flux tends to increase for fast solar wind ( $V_{sw} > 500$  km/s) for CME storms at  $L = 3$ . The dependence on  $V_{sw}$  is weaker than that for the CIR storm at  $L = 5$ . The

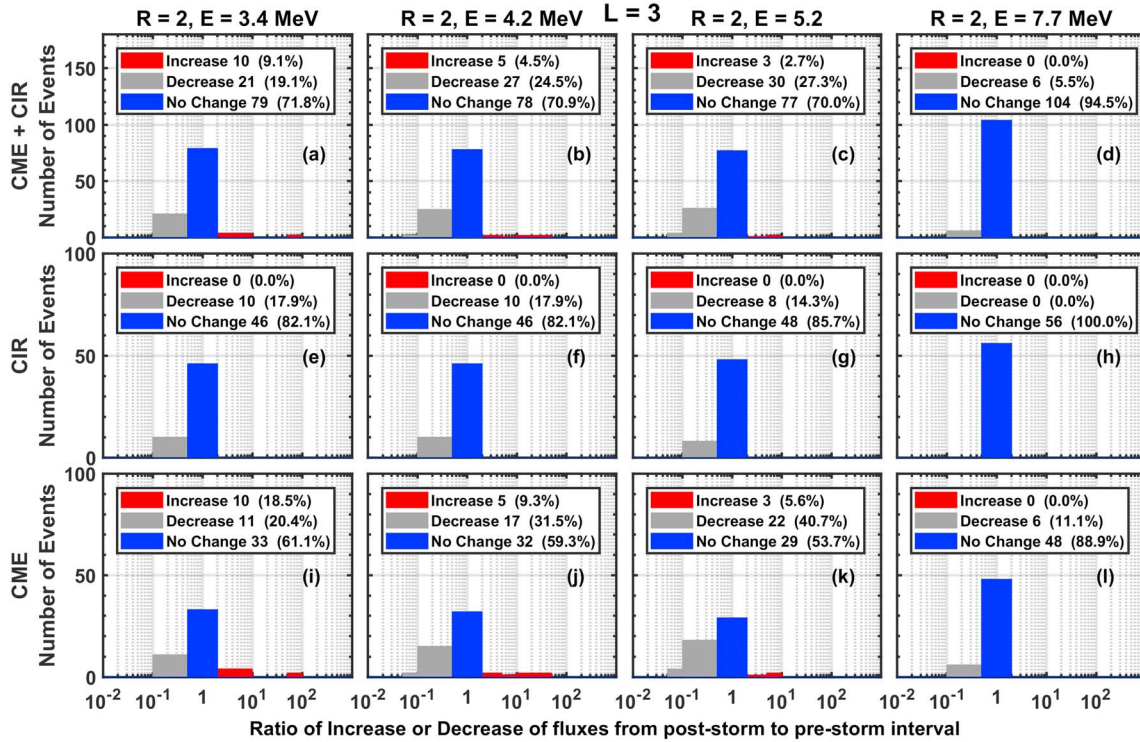


**Figure 6.** Histograms of the rate of the change in the electron flux between the poststorm interval and the prestorm interval for the CME- and CIR-driven geomagnetic storms at  $L = 3$  for 3.4- to 7.7-MeV energy channels. When the rate of change falls within a factor of 2, we call it “no change.” When the rate is larger (smaller) than 2, we consider it as “increase” (“decrease”). (a–d) The histograms for the CME- and CIR-driven storms. (e–h) The CIR-driven storms and (i–l) the CME-driven geomagnetic storms. CIR = corotating interaction region; CME = coronal mass ejection.

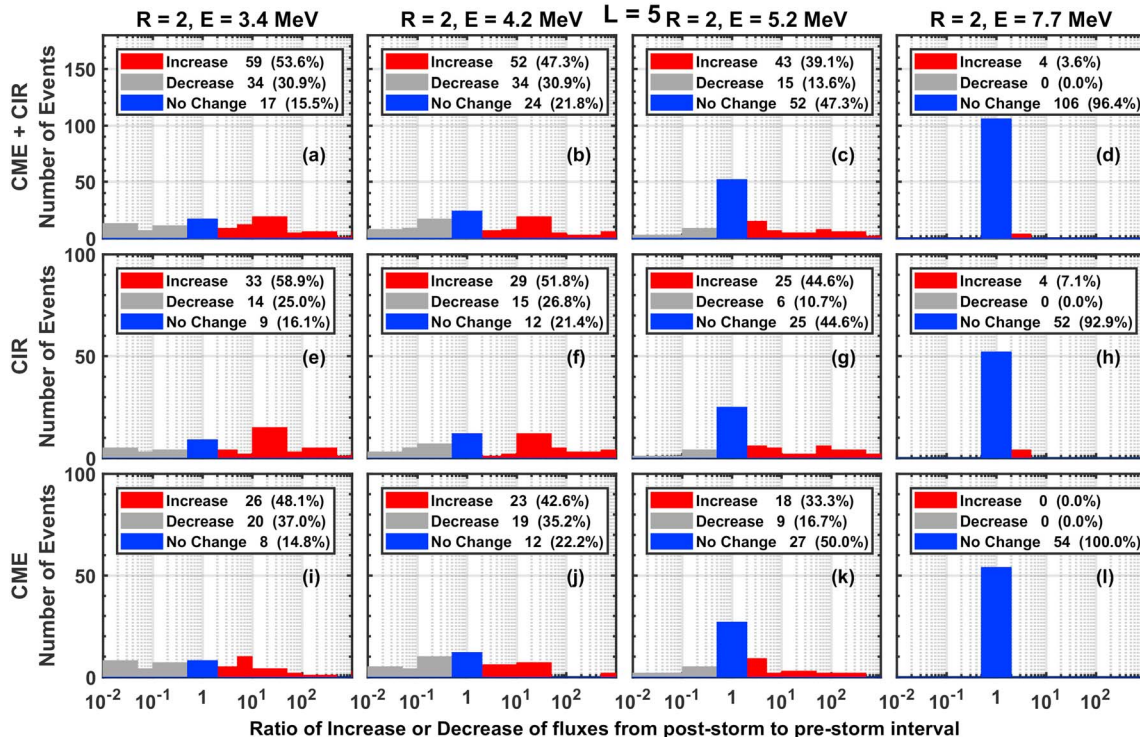


**Figure 7.** Same as Figure 6 except for  $L = 5$ .

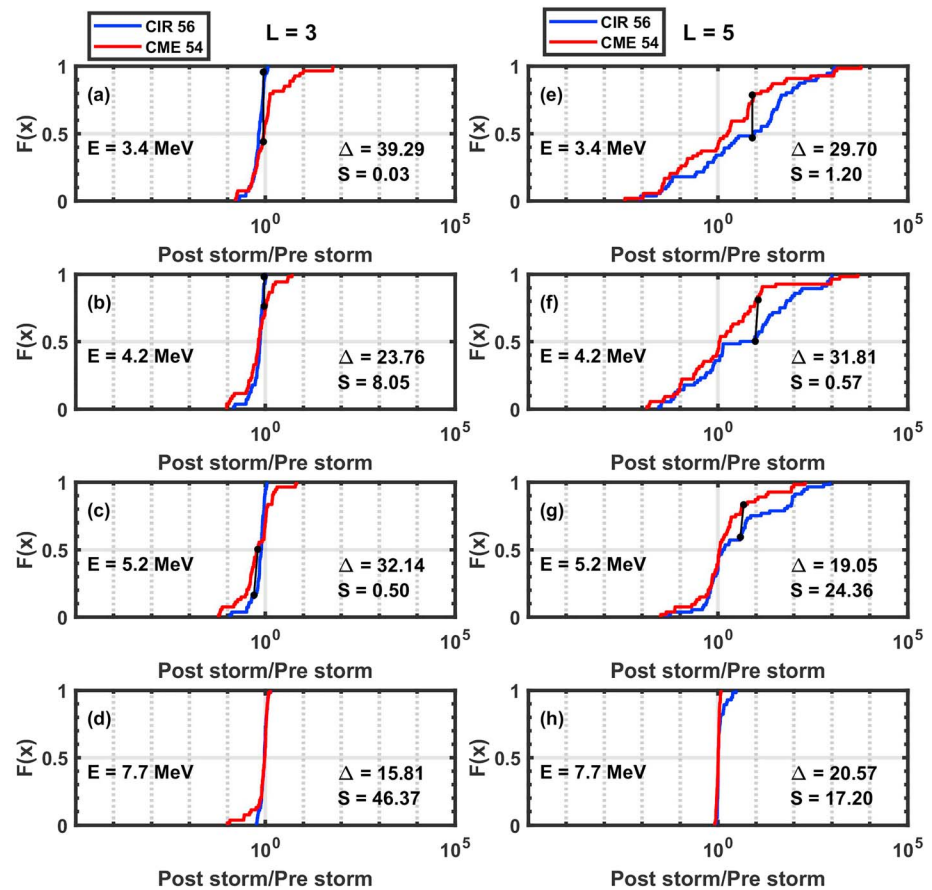


**Figure 8.** Cumulative probability distribution of poststorm to prestorm flux ratios binned according to CME- (red) or CIR- (blue) driven geomagnetic storm at  $L = 3$  (a–d) and  $L = 5$  (e–h). Here we have a total of 56 observations for 28 CIR storms and 54 observations for 27 CME-driven magnetic storms. The panels represent different energy channels at a given  $L$ -value. The black line in each panel represents the value of  $\Delta$ . CIR = corotating interaction region; CME = coronal mass ejection.

dependence on  $P_{sw}$  is weak for the CME- and CIR-driven storms. The dependence on  $Sym-H$  is somewhat weak for the CME-driven storms, whereas it is large for the CIR-driven storms (Figure 10).

#### 4. Discussion

In our studies, we continue to extend the existing picture of the radiation belt electron flux variability in the Earth's magnetosphere by analyzing the Van Allen Probes-REPT data from October 2012 to May 2017. We statistically examined electron flux variations in the energy range of 3.4–7.7 MeV for 55 magnetic storms having minimum  $Sym-H < -50$  nT. Further, we classified these magnetic storms based on their respective solar sources (CME and CIR) and categorized flux variability as enhancement, depletion, or no change based on the electron flux observed at each  $L$ -value and each energy channel. We summarize the results, in Table 2, from other previous investigations and compare the outcome to get a substantial understanding of electron flux variation during magnetic storms. Our study extends previous studies and provides some new insights to the current understanding of electron flux response to IP drivers.

For the considered range of energies, we find that the response of electron flux varies differently for the CME-driven and CIR-driven storms at each  $L$ -value and interval of the storm and related solar wind parameters. At  $L = 3$ , the CME-driven storms show higher flux enhancements at lower energies (3.4–5.2 MeV) than CIR storms, while no significant change is observed for higher energies (7.7 MeV; Figure 6). This could be attributed to the strong plasmasphere erosion and a favorable condition for chorus waves to be excited at low  $L$ -shell [e.g., Baker et al. 2004; Thorne et al., 2013]. On the other hand, it is found that, for  $L = 5$ , the flux

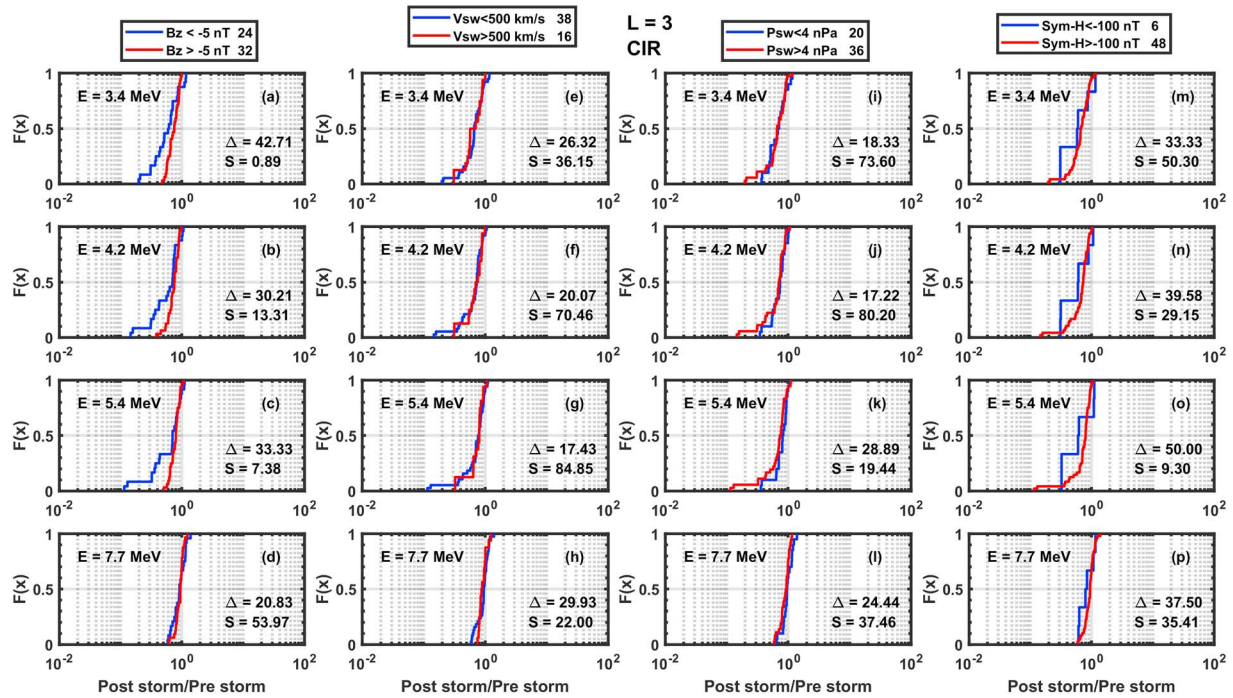


**Figure 9.** Cumulative probability distribution of poststorm to prestorm flux ratios for corotating interaction region-driven magnetic storms at  $L = 3$ . They are binned according to (a–d)  $B_z$ , (e–h) solar wind velocity, (i–l) solar wind dynamic pressure, and (m–o) strength of magnetic activity. The distributions are scaled at different energies from 3.4–7.7 MeV. The color code corresponding to each is given at the top of their respective panels.

enhancements are more for CIR-driven storms than for CME up to 5.2 MeV. Irrespective of the storm driver, the total percentage of the no change flux events decreases with the increasing  $L$ -value, that is, from  $L = 3$  (70–90%) to  $L = 5$  (15–90%) depending upon its energies. It is very much noticeable that there is a

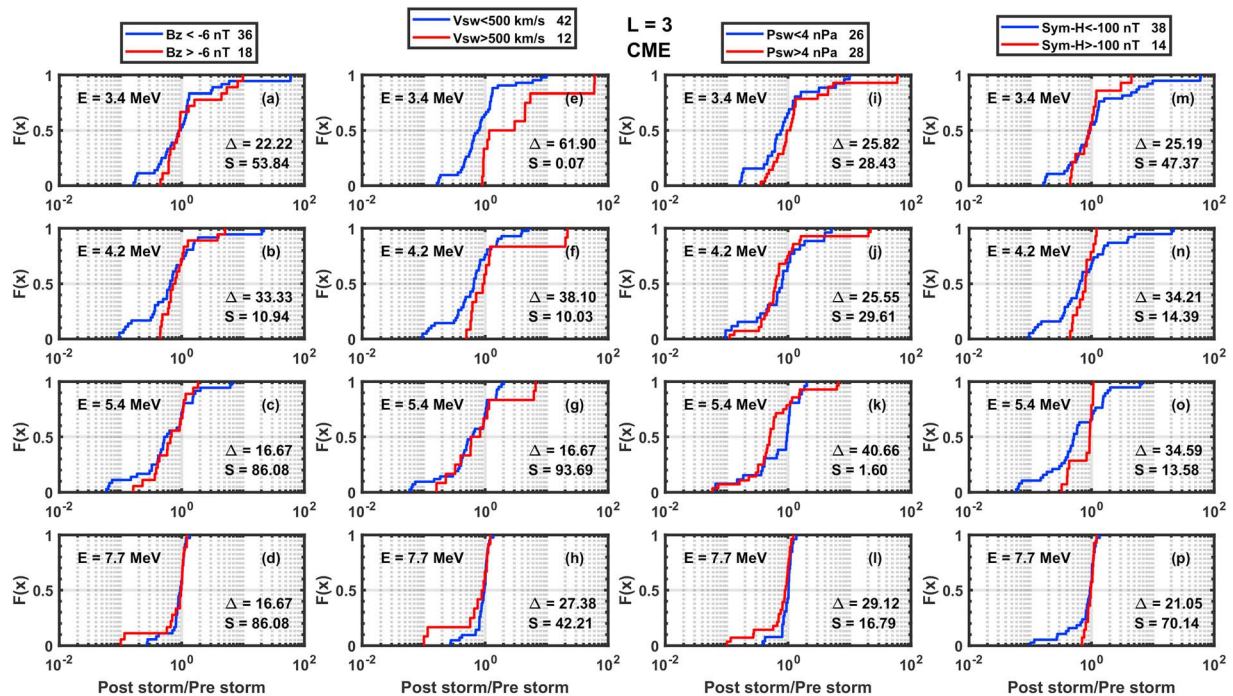


**Figure 10.** Same as Figure 9 except for  $L = 5$ . CME = coronal mass ejection.

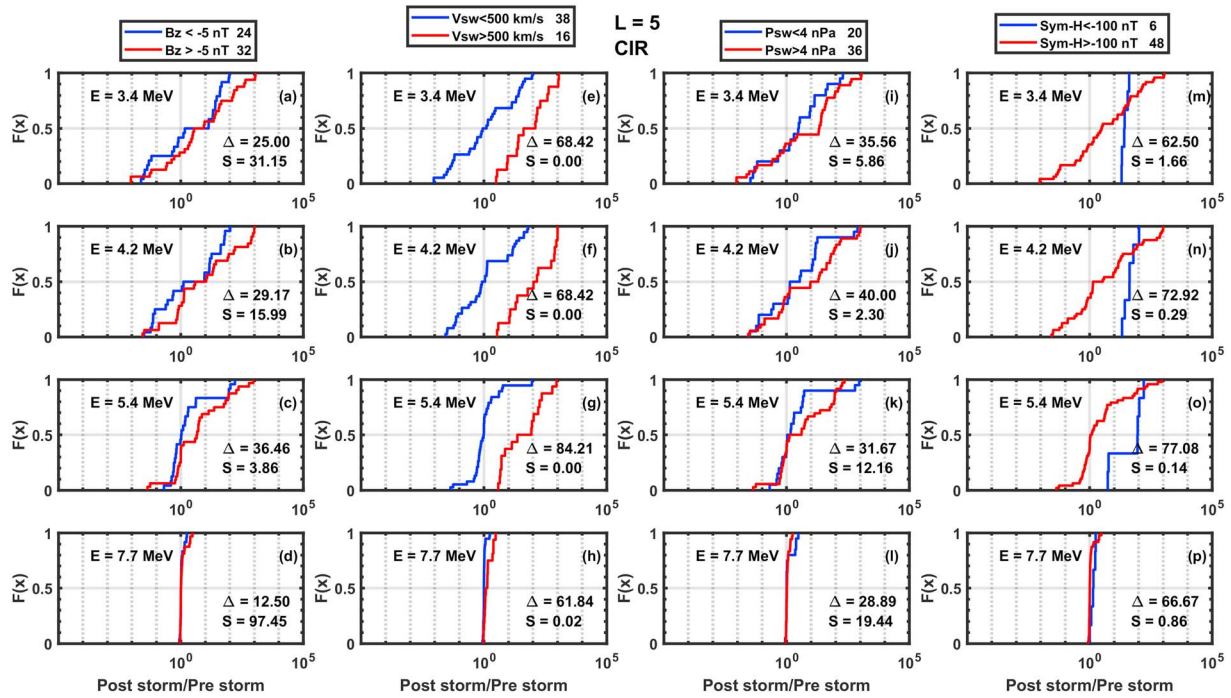


Figure 11. Same as Figure 9 except for the coronal mass ejection-driven magnetic storms. CIR = corotating interaction region.

significant probability of flux enhancement for CIR-driven storms than CME, in particular for  $L = 5$  (Figure 8). The CME and CIR storm response using GOES spacecraft at  $L = 6.6$  by super epoch analysis and found that CIRs are significantly more effective for the evolution of the outer belt electrons than CMEs, due to existence of a series of particle injections driven by Alfvén waves within the fast coronal

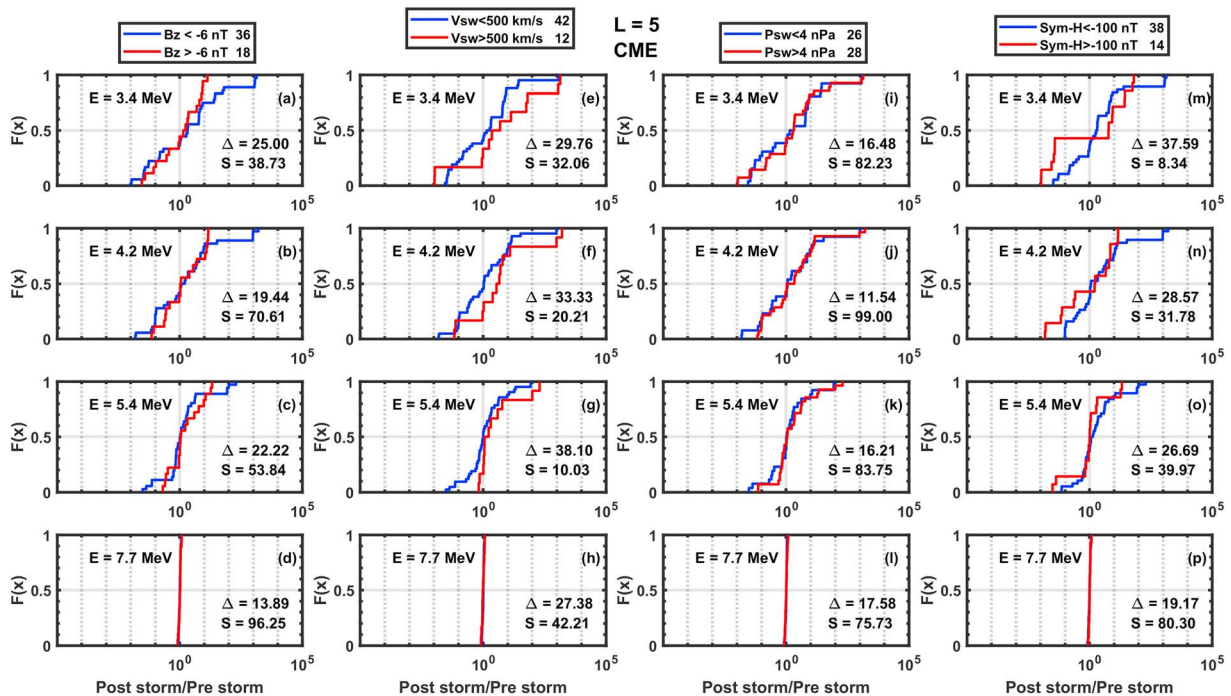


Figure 12. Same as Figure 10 except the coronal mass ejection (CME)-driven magnetic storms.

**Table 2**

Summary of the Previous and Recent Studies of Radiation Belt Electron Flux During Geomagnetic Storms, Which Are Focused on CME- and CIR-Driven Storms

Reference	<i>L</i> -value surveyed	Energy surveyed	Solar sources category	Spacecraft used	Total no. of storms	Outcomes
O'Brien et al. (2001)	~6.6	0.3–1.5 MeV	Not categorized	GOES LANL	62	Sustained solar wind velocity >450 km/s increases relativistic electrons.
Reeves et al. (2003)	~6.6	1–3 MeV	Not categorized	POLAR	276	Relativistic electron flux shows an increase, a decrease, or unchanged after a geomagnetic storm. Dependence of electron flux enhancements on <i>V</i> <sub>sw</sub> is shown.
Miyoshi and Kataoka (2005)	>1 and ~6.6	>300 keV	CME + CIR	NOAA-12 and GOES	78	CME-driven storms are effective at enhancing the subrelativistic electron flux (>300 keV) at $L \leq 3$ , while CIR-driven storms are the most effective for rebuilding the subrelativistic electron flux at $L > 3.5$ .
Yuan and Zong (2012)	>1	1.5–6 MeV	CME + CIR	SAMPEX	80	CME-driven storms produce more relativistic electrons than CIR-driven storms.
Miyoshi et al. (2013)	>2 and ~6.6	>2.5 MeV	CIR	Akebono and GOES	108	HSS events with the southward IMF are dominant for the relativistic electron acceleration by whistler mode waves than the events with the northward IMF
Hietala et al. (2014)	~6.6	>2 MeV	CME	GOES	31	CME sheaths are effective at depleting the relativistic electron flux.
Anderson et al. (2015)	~6.6	1.8–3.5 MeV	Not categorized	LANL	576	<i>Dst</i> is a poor indicator of the relativistic electron dynamics
Turner et al. (2015)	2.5–6	Tens of kiloelectron volts to 2 MeV	Not categorized	Van Allen Probes	52	At $E \geq 1$ MeV, the results are quite evenly distributed between enhancements, depletions, and no-change events at $L > 4$ . At $L < 4$ , most events result in no change.
Kilpua et al. (2015)	3–6 and ~6.6	0.06–1.5 MeV	CME + CIR	Van Allen Probe and GOES	193	The electrons are depleted for CME ejecta and sheaths while enhancements occur during fast streams trailing the stream interface or the CME.
Shen et al. (2017)	3–5	>1 MeV	CME + CIR	Van Allen Probes	59	CIR-driven storms have a greater effect at geosynchronous orbit than CME-driven storms especially for $E > 2$ MeV
Moya et al. (2017)	6	1.8 MeV	Not categorized	Van Allen Probes	78	Depletion are more probable for 4- to 5-MeV electrons in the outer radiation belt, and no-change events are more frequent at $L < 3.5$ for $E \sim 3$ -MeV particles.
Murphy et al. (2018)	3–6	300 keV to 2.5 MeV	CME	Van Allen Probes	73	Electron loss is mainly dominated during the main phase by the electron loss while the acceleration/source is dominated during the recovery phase
Turner et al. (2019)	2.5–6	30 keV to 6.3 MeV	CME + CIR	Van Allen Probes	110	CME shocks/sheaths and ejecta result in a depletion of >1-MeV electrons for $L < 5$ . Storms driven by full CMEs and CIRs produce an enhancement of megaelectron volt electrons at $L > 4.5$

Note. CIR = corotating interaction region; CME = coronal mass ejection; HSS = high-speed solar wind streams; IMF = interplanetary magnetic field.

hole stream following the CIR [Miyoshi and Kataoka (2005)]. Recently, Turner et al. (2019) studied the electron flux variation during 110 magnetic storms driven by CME and CIR at different *L*-values for the band of 30 keV to 6.3 MeV. They found that at energies >1 MeV, for CIR storms, more electron flux is enhanced at  $L > \sim 4.5$  and for CME storms at  $L < 5$ . This is in accordance with our results that, at  $L = 3$  increase of the electron flux was observed only for the CME-driven storms, while at  $L = 5$  for CIR storms.

In the present study we determined the preferential IMF parameters leading to megaelectron volt electron enhancements for different solar wind parameters at different *L*-value and energies. We show that high

solar wind velocity is one of the major factors leading to the electron flux enhancement at  $L = 5$ . The post-storm of electron flux enhances at all the energies with the increasing  $V_{sw}$ . The effects are more distinct in case of CIR-driven storms. The CME-driven magnetic storms at  $L = 3$  also shows the electron flux increase with the increasing  $V_{sw}$ . This results are consistent with the previous results by Baker et al. (1997), Kanekal et al. (1999), Reeves et al. (2003, 2011), and Yuan and Zong (2013), in which magnetic storms are not categorized. Additionally, we found that, the enhancement of the relativistic electron flux is relatively associated with  $V_{sw}$  than IMF  $B_z$  at  $L = 5$ , whereas it is associated with IMF  $B_z$  than  $V_{sw}$  at  $L = 3$ . For southward IMF  $B_z$  ( $< -6$  nT), the electron flux enhances and it is more prominent for CME-driven storms at  $L = 5$  (Figure 12). Further, Li et al. (2011) studied that southward IMF  $B_z$  is the essential condition for the electron flux enhancements and selection of criteria of solarwind parameters is utmost important to study the related flux variations. Recently, Aryan et al. (2014) studied that a large chorus intensities are observed during active conditions having high  $V_{sw}$ , low solar wind densities, high  $P_{sw}$ , and high IMF  $B_z$ . Moreover, this is found to be consistent with recently developed a multiparameter chorus and plasmaspheric hiss wave models based on geomagnetic index and solar wind parameters (Aryan et al., 2017). Chorus wave activities largely depend on solar wind speed and southward IMF  $B_z$  strength. Very recently, Zhao et al. (2019) concluded that higher solar wind speed, prolonged southward IMF  $B_z$ , and lower number density could be the possible reasons for enhancement of electron flux in outer belt for magnetic storms, which are not classified as CME or CIR. Iles et al. (2002) showed that the main requirement for electron flux enhancement and generation of whistler mode waves during a recovery phase is the fast solar wind and predominant southward IMF  $B_z$  or fluctuating around zero. Recently, Yuan and Zong (2019) categorized CMEs into four types according to  $B_z$  direction upstream of IP shock, at sheath region and within CME. They quantified the variations of 1.8- to 7.7-MeV electrons and found that continuous southward IMF  $B_z$  from upstream of shock to CME leading edge cause a prominent enhancements of megaelectron volt electrons, while continuous northward IMF  $B_z$  from upstream of shock to CME leading edge results in depletion of megaelectron volt electrons.

We studied the dependence of the change in the relativistic electron flux on *Sym-H* at particular  $L$ -shell and energy for CME and CIR storms. Our results clearly show that the intensity of storm (as seen by *Sym-H*) significantly result in the increase of electron flux at  $L = 3$  and 5 for CIR storms, while weaker strength noticed for CME storms. Our study reveals the probability of electron flux variations in terms of the averaged solar wind parameters and the storm drivers at  $L = 3$  and 5. There are several mechanisms involved in the electron flux variations like, magnetopause shadowing (Bortnik et al., 2006), radial transport by ULF waves (Rostoker et al., 1998), interaction with chorus waves (Horne & Thorne, 1998; Li et al., 2015; Summers et al., 1998; Thorne et al., 2013), and interaction with electromagnetic ion cyclotron waves [Baker et al., 2019; Summers & Ma, 2000; Turner et al., 2019, and references there in]. In particular, nonlinear interaction with electromagnetic ion cyclotron waves is suggested to cause scattering of relativistic electrons very rapidly, resulting in precipitation into the upper atmosphere (Omura & Zhao, 2012). The clear attribution of any mechanism for electron flux enhancements or dropouts is beyond scope of our study. However, our statistical results will provide an important input to test model studies in particular for CIR- and CME-driven geomagnetic storms for electron flux with the energies of  $>3.4$  MeV.

## 5. Summary

When we compare the prestorm and poststorm fluxes, the significant outcomes of the studies are the following: (i) At  $L = 3$ , we found that for  $>70\%$  of the total geomagnetic storms, the electron flux remains unchanged at all the energy channels. (ii) When compared with CME storms, CIR-driven magnetic storms do not significantly affect the electron flux at  $L = 3$  ( $>82\%$  magnetic storms show no change). (iii) At  $L = 5$ , for  $>80\%$  of the magnetic storms, the fluxes changes at  $E = 3.4$  MeV. However, the electron flux variation decreases with the increasing energies. (iv) Out of the total flux variation at  $L = 5$  and  $E = 3.4$  MeV,  $\sim 53\%$  increased and  $\sim 30\%$  decreased. Out of the total flux increases  $\sim 56\%$  is from CIR storms, while  $\sim 44\%$  is from CME-driven magnetic storms. (v) Poststorm electron flux is basically independent of the prestorm flux. (vi) Solar wind speed ( $V_{sw}$ ) is crucial for the electron flux enhancements. The poststorm electron flux, especially, at  $L = 5$  for CIR-driven magnetic storms, increases with  $V_{sw}$ . At higher energies, especially  $>5.4$  MeV, the role of  $V_{sw}$  for electron flux enhancement diminishes. (vii) At  $L = 3$  for CIR-driven storms, magnitude of IMF  $B_z$  and *Sym-H* is also considered as another important parameter that helps electron flux enhancement. (viii) The electron flux variation is largely dependent on storm strength (*Sym-H*) in particularly for CIR-

driven storms at  $L = 5$ . Our results highlight the importance of understanding electron loss and acceleration processes during geomagnetic storms. Electron flux observed during the magnetic storms is a delicate balance between the amount of acceleration and the amount of loss.

### Acknowledgments

This work is supported by the Department of Science and Technology, Government of India. Part of this study is supported by JSPS KAKENHI Grants 15H03732 and 15H05815. We sincerely thank G. D. Reeves for very constructive and healthy discussion during AP-RASC URSI-2019 meeting. The authors are thankful to all of the Van Allen Probes, ACE, Wind, and Kyoto World Data Center for Geomagnetism teams for making their data available to the public. In addition to coauthors' contributions, we thank ACE, Wind, and OMNI: J. H. King, N. Papatashvilli, and team for OMNI solar wind data; and NASA CDAWeb and mission specific online databases. We thank the Los Alamos National Laboratory, USA (<http://www.rbsp-ect.lanl.gov/>) for providing the Van Allen Probes ECT data. SYM-H data are available from the website (<http://omniweb.gsfc.nasa.gov>).

### References

- Anderson, B. R., Millan, R. M., Reeves, G. D., & Friedel, R. H. W. (2015). Acceleration and loss of relativistic electrons during small geomagnetic storms. *Geophysical Research Letters*, *42*, 10,113–10,119. <https://doi.org/10.1002/2015GL066376>
- Aryan, H., Sibeck, D. G., Kang, S.B., Balikhin, M. A., Fok, M. C., Agapitov, O., Komar, C. M., Kanekal, S. G., & Nagai, T. (2017). CIMI simulations with newly developed multiparameter chorus and plasmaspheric hiss wave models. *Journal of Geophysical Research: Space Physics*, *122*, 9344–9357. <https://doi.org/10.1002/2017JA024159>
- Aryan, H., Yearby, K., Balikhin, M., Agapitov, O., Krasnoselskikh, V., & Boynton, R. (2014). Statistical study of chorus wave distributions in the inner magnetosphere using Ae and solar wind parameters. *Journal of Geophysical Research: Space Physics*, *119*, 6131–6144. <https://doi.org/10.1002/2014JA019939>
- Baker, D. N., Higbie, P. R., Belian, R. D., & Hones, E. W. (1979). Do Jovian electrons influence the terrestrial outer radiation zone? *Geophysical Research Letters*, *6*(6), 531–534. <https://doi.org/10.1029/GL0061006p00531>
- Baker, D. N., Hoxie, V., Zhao, H., Jaynes, A. N., Kanekal, S., Li, X., & Elkington, S. (2019). Multiyear measurements of radiation belt electrons: Acceleration, transport, and loss. *Journal of Geophysical Research: Space Physics*, *124*, 2588–2602. <https://doi.org/10.1029/2018JA026259>
- Baker, D. N., Jaynes, A. N., Hoxie, V. C., Thorne, R. M., Foster, J. C., Li, X., et al. (2014). An impenetrable barrier to ultrarelativistic electrons in the Van Allen radiation belts. *Nature*, *515*(7528), 531–534. <https://doi.org/10.1038/nature13956>
- Baker, D. N., & Kanekal, S. G. (2008). Solar cycle changes, geomagnetic variations, and energetic particle properties in the inner magnetosphere. *Journal of Atmospheric and Solar - Terrestrial Physics*, *70*(2–4), 195–206. <https://doi.org/10.1016/j.jastp.2007.08.031>
- Baker, D. N., Kanekal, S. G., Hoxie, V. C., Batiste, S., Bolton, M., Li, X., et al. (2012). The Relativistic Electron-Proton Telescope (REPT) instrument on board the Radiation Belt Storm Probes (RBSP) spacecraft: Characterization of Earth's radiation belt high-energy particle populations. In *The Van Allen Probes Mission*, (pp. 337–381). Boston, MA: Springer.
- Baker, D. N., Kanekal, S. G., Li, X., Monk, S. P., Goldstein, J., & Burch, J. L. (2004). An extreme distortion of the Van Allen belt arising from the 'Halloween' solar storm in 2003. *Nature*, *432*(7019), 878–881. <https://doi.org/10.1038/nature03116>
- Baker, D. N., Li, X., Turner, N., Allen, J. H., Bargatze, L. F., Blake, J. B., Sheldon, R. B., Spence, H. E., Belian, R. D., Reeves, G. D., Kanekal, S. G., Klecker, B., Lepping, R. P., Ogilvie, K., Mewaldt, R. A., Onsager, T., Singer, H. J., & Rostoker, G. (1997). Recurrent geomagnetic storms and relativistic electron enhancements in the outer magnetosphere: ISTP coordinated measurements. *Journal of Geophysical Research*, *102*(A7), 14,141–14,148. <https://doi.org/10.1029/97JA00565>
- Baker, D. N., Pulkkinen, T. I., Li, X., Kanekal, S. G., Ogilvie, K. W., Lepping, R. P., et al. (1998). A strong CME-related magnetic cloud interaction with the Earth's magnetosphere: ISTP observations of rapid relativistic electron acceleration on May 15, 1997. *Geophysical Research Letters*, *25*(15), 2975–2978. <https://doi.org/10.1029/98GL01134>
- Blake, J. B., Baker, D. N., Turner, N., Ogilvie, K. W., & Lepping, R. P. (1997). Correlation of changes in the outer-zone relativistic-electron population with upstream solar wind and magnetic field measurements. *Geophysical Research Letters*, *24*(8), 927–929. <https://doi.org/10.1029/97GL00859>
- Blake, J. B., Kolasinski, W. A., Fillius, R. W., & Mullen, E. G. (1992). Injection of electrons and protons with energies of tens of MeV into  $L < 3$  on March 24, 1991. *Geophysical Research Letters*, *19*(8), 821–824. <https://doi.org/10.1029/92GL00624>
- Bortnik, J., Thorne, R. M., O'Brien, T. P., Green, J. C., Strangeway, R. J., Shprits, Y. Y., & Baker, D. N. (2006). Observation of two distinct, rapid loss mechanisms during the 20 November 2003 radiation belt dropout event. *Journal of Geophysical Research*, *111*, A12216. <https://doi.org/10.1029/2006JA011802>
- Borovsky, J. E., & Denton, M. H. (2006). Differences between CME-driven storms and CIR-driven storms. *Journal of Geophysical Research*, *111*, A07S08. <https://doi.org/10.1029/2005JA011447>
- Denton, M. H., Borovsky, J. E., Skoug, R. M., Thomsen, M. F., Lavraud, B., Henderson, M. G., et al. (2006). Geomagnetic storms driven by ICME- and CIR-dominated solar wind. *Journal of Geophysical Research*, *111*, A07S07. <https://doi.org/10.1029/2005JA011436>
- Friedel, R. H. W., Reeves, G. D., & Obara, T. (2002). Relativistic electron dynamics in the inner magnetosphere—A review. *Journal of Atmospheric and Solar - Terrestrial Physics*, *64*(2), 265–282. [https://doi.org/10.1016/S1364-6826\(01\)00088-8](https://doi.org/10.1016/S1364-6826(01)00088-8)
- Hao, Y. X., Zong, Q.G., Zhou, X.Z., Rankin, R., Chen, X. R., Liu, Y., et al. (2019). Global-scale ULF waves associated with SSC accelerate magnetospheric ultra relativistic electrons. *Journal of Geophysical Research: Space Physics*, *124*, 1525–1538. <https://doi.org/10.1029/2018JA026134>
- Hietala, H., Kilpua, E. K. J., Turner, D. L., & Angelopoulos, V. (2014). Depleting effects of ICME-driven sheath regions on the outer electron radiation belt. *Geophysical Research Letters*, *41*, 2258–2265. <https://doi.org/10.1002/2014GL059551>
- Horne, R. B., & Thorne, R. M. (1998). Potential waves for relativistic electron scattering and stochastic acceleration during magnetic storms. *Geophysical Research Letters*, *25*(15), 3011–3014. <https://doi.org/10.1029/98GL01002>
- Iles, R. H. A., Fazakerley, A. N., Johnstone, A. D., Meredith, N. P., & Bühler, P. (2002). The relativistic electron response in the outer radiation belt during magnetic storms. *Annales Geophysicae*, *20*(7), 957–965.
- Jaynes, A. N., Baker, D. N., Singer, H. J., Rodriguez, J. V., Loto'aniu, T. M., Ali, A. F., et al. (2015). Source and seed populations for relativistic electrons: Their roles in radiation belt changes. *Journal of Geophysical Research: Space Physics*, *120*, 7240–7254. <https://doi.org/10.1002/2015JA021234>
- Kanekal, S. G. (2006). A review of recent observations of relativistic electron energization in the Earth's outer Van Allen radiation belt. In N. Gopalswamy, & A. Bhattacharyya (Eds.), *Proceedings of the ILWS Workshop on Solar Influence on the Heliosphere and Earth's Environment*, (pp. 274–279). Goa, India: Quest Publishers.
- Kanekal, S. G., Baker, D. N., Blake, J. B., Klecker, B., Mewaldt, R. A., & Mason, G. M. (1999). Magnetospheric response to magnetic cloud (coronal mass ejection) events: Relativistic electron observations from SAMPEX and Polar. *Journal of Geophysical Research*, *104*(A11), 24,885–24,894.
- Kanekal, S. G., Baker, D. N., Fennell, J. F., Jones, A., Schiller, Q., Richardson, I. G., et al. (2016). Prompt acceleration of magnetospheric electrons to ultrarelativistic energies by the 17 March 2015 interplanetary shock. *Journal of Geophysical Research: Space Physics*, *121*, 7622–7635. <https://doi.org/10.1002/2016JA022596>

- Kanekal, S. G., Baker, D. N., Henderson, M. G., Li, W., Fennell, J. F., Zheng, Y., et al. (2015). Relativistic electron response to the combined magnetospheric impact of a coronal mass ejection overlapping with a high-speed stream: Van Allen Probes observations. *Journal of Geophysical Research: Space Physics*, *120*, 7629–7641. <https://doi.org/10.1002/2015JA021395>
- Kang, S.-B., Fok, M.-C., Komar, C., Glocher, A., Li, W., & Buzulukova, N. (2018). An energetic electron flux dropout due to magnetopause shadowing on 1 June 2013. *Journal of Geophysical Research: Space Physics*, *123*, 1178–1190. <https://doi.org/10.1002/2017JA024879>
- Kataoka, R., & Miyoshi, Y. (2006). Flux enhancement of radiation belt electrons during geomagnetic storms driven by coronal mass ejections and corotating interaction regions. *Advances in Space Research*, *4*(9). <https://doi.org/10.1029/2005SW000211>
- Kilpua, E. K. J., Hietala, H., Turner, D. L., Koskinen, H. E. J., Pulkkinen, T. I., Rodriguez, J. V., et al. (2015). Unraveling the drivers of the storm time radiation belt response. *Geophysical Research Letters*, *42*, 3076–3084. <https://doi.org/10.1002/2015GL063542>
- Kim, H.-J., & Chan, A. A. (1997). Fully adiabatic changes in storm time relativistic electron fluxes. *Journal of Geophysical Research*, *102*(A10), 22,107–22,116. <https://doi.org/10.1029/97JA01814>
- Kim, H.-J., Kim, K. C., Lee, D., & Rostoker, G. (2006). Origin of geosynchronous relativistic electron events. *Journal of Geophysical Research*, *111*, A03208. <https://doi.org/10.1029/2005JA011469>
- King, J. H., & Papitashvili, N. E. (2005). Solar wind spatial scales in and comparisons of hourly Wind and ACE plasma and magnetic field data. *Journal of Geophysical Research*, *110*, A02104. <https://doi.org/10.1029/2004JA010649>
- Li, W., Thorne, R. M., Bortnik, J., Baker, D. N., Reeves, G. D., Kanekal, S. G., et al. (2015). Solar wind conditions leading to efficient radiation belt electron acceleration: A superposed epoch analysis. *Geophysical Research Letters*, *42*, 6906–6915. <https://doi.org/10.1002/2015GL065342>
- Li, X., Baker, D. N., Temerin, M., Reeves, G., Friedel, R., & Shen, C. (2005). Energetic electrons, 50 keV to 6 MeV, at geosynchronous orbit: Their responses to solar wind variations. *Space Weather*, *3*, S04001. <https://doi.org/10.1029/2004SW000105>
- Li, X., Roth, I., Temerin, M., Wygant, J. R., Hudson, M. K., & Blake, J. B. (1993). Simulation of the prompt energization and transport of radiation belt particles during the March 24, 1991 SSC. *Geophysical Research Letters*, *20*(22), 2423–2426. <https://doi.org/10.1029/93GL02701>
- Li, X., Temerin, M., Baker, D. N., & Reeves, G. D. (2011). Behavior of MeV electrons at geosynchronous orbit during last two solar cycles. *Journal of Geophysical Research*, *116*, A11207. <https://doi.org/10.1029/2011JA016934>
- Marcia, N., & Raymond, G. (1997). Particle and field signatures of coronal mass ejections in the solar wind. In N. Crooker, J. A. Joselyn, & J. Feynman (Eds.), *Coronal mass Ejections*, (pp. 245–251). Washington, D. C.: American Geophysical Union.
- Mauk, B. H., Fox, N. J., Kanekal, S. G., Kessel, R. L., Sibeck, D. G., & Ukhorskiy, A. (2014). Science objectives and rationale for the Radiation Belt Storm Probes mission. *Space Science Reviews*, *179*, 3–27. [https://doi.org/10.1007/978-1-4899-7433-4\\_2](https://doi.org/10.1007/978-1-4899-7433-4_2)
- McLwain, C. E. (1966). Ring current effects on trapped particles. *Journal of Geophysical Research*, *71*(15), 3623–3628. <https://doi.org/10.1029/JZ071i015p03623>
- Miyoshi, Y., & Kataoka, R. (2005). Ring current ions and radiation belt electrons during geomagnetic storms driven by coronal mass ejections and corotating interaction regions. *Geophysical Research Letters*, *32*, L21105. <https://doi.org/10.1029/2005GL024590>
- Miyoshi, Y., Kataoka, R., Kasahara, Y., Kumamoto, A., Nagai, T., & Thomsen, M. F. (2013). High-speed solar wind with southward interplanetary magnetic field causes relativistic electron flux enhancement of the outer radiation belt via enhanced condition of whistler waves. *Geophysical Research Letters*, *40*, 4520–4525. <https://doi.org/10.1002/grl.50916>
- Miyoshi, Y., Morioka, A., Kataoka, R., Kasahara, Y., & Mukai, T. (2007). Evolution of the outer radiation belt during the November 1993 storms driven by corotating interaction regions. *Journal of Geophysical Research*, *112*, A05210. <https://doi.org/10.1029/2006JA012148>
- Miyoshi, Y., Morioka, A., Misawa, H., Obara, T., Nagai, T., & Kasahara, Y. (2003). Rebuilding process of the outer radiation belt during the 3 November 1993 magnetic storm: NOAA and Exos-D observations. *Journal of Geophysical Research*, *108*(A1), 1004. <https://doi.org/10.1029/2001JA007542>
- Moya, P. S., Pinto, V. A., Sibeck, D. G., Kanekal, S. G., & Baker, D. N. (2017). On the effect of geomagnetic storms on relativistic electrons in the outer radiation belt: Van Allen Probes observations. *Journal of Geophysical Research: Space Physics*, *122*, 11,100–11,108. <https://doi.org/10.1002/2017JA024735>
- Murphy, K. R., Watt, C. E. J., Mann, I. R., Jonathan Rae, I., Sibeck, D. G., Boyd, A. J., et al. (2018). The global statistical response of the outer radiation belt during geomagnetic storms. *Geophysical Research Letters*, *45*, 3783–3792. <https://doi.org/10.1002/2017GL076674>
- Nakamura, R., Kamei, K., Kamide, Y., Baker, D., Blake, J., & Looper, M. (1998). SAMPEX observations of storm-associated electron flux variations in the outer radiation belt. *Journal of Geophysical Research*, *103*(A11), 26,261–26,269. <https://doi.org/10.1029/97JA02873>
- O'Brien, T. P., McPherron, R. L., Sornette, D., Reeves, G. D., Friedel, R., & Singer, H. J. (2001). Which magnetic storms produce relativistic electrons at geosynchronous orbit? *Journal of Geophysical Research*, *106*(A8), 15,533–15,544.
- Omura, Y., & Zhao, Q. (2012). Nonlinear pitch angle scattering of relativistic electrons by EMIC waves in the inner magnetosphere. *Journal of Geophysical Research*, *117*, A08227. <https://doi.org/10.1029/2012JA017943>
- Paulikas, G. A., & Blake, J. B. (1979). Effects of the solar wind on magnetospheric dynamics: Energetic electrons at the synchronous orbit. In W. P. Olson (Ed.), *Quantitative modeling of magnetospheric processes*, *Geophys. Monogr. Ser.*, (Vol. 21, pp. 180–202). Washington, D. C.: American Geophysical Union.
- Press, W. H., Teukolsky, S. A., Vetterling, W. T., & Flannery, B. P. (2007). *Numerical recipes 3rd edition: The art of scientific computing*. Cambridge: Cambridge University Press.
- Reeves, G. D., McAdams, K. L., Friedel, R. H. W., & O'Brien, T. P. (2003). Acceleration and loss of relativistic electrons during geomagnetic storms. *Geophysical Research Letters*, *30*(10), 1529. <https://doi.org/10.1029/2002GL016513>
- Reeves, G. D., Morley, S. K., Friedel, R. H., Henderson, M. G., Cayton, T. E., Cunningham, G., et al. (2011). On the relationship between relativistic electron flux and solar wind velocity: Paulikas and Blake revisited. *Journal of Geophysical Research*, *116*, A02213. <https://doi.org/10.1029/2010JA015735>
- Rostoker, G., Skone, S., & Baker, D. N. (1998). On the origin of relativistic electrons in the magnetosphere associated with some geomagnetic storms. *Geophysical Research Letters*, *25*(19), 3701–3704. <https://doi.org/10.1029/98GL02801>
- Shen, X.-C., Hudson, M. K., Jaynes, A., Shi, Q., Tian, A., Claudepierre, S., et al. (2017). Statistical study of the storm time radiation belt evolution during Van Allen Probes era: CME- versus CIR-driven storms. *Journal of Geophysical Research: Space Physics*, *122*, 8327–8339. <https://doi.org/10.1002/2017JA024100>
- Shprits, Y. Y., Kellerman, A., Aseev, N., Drozdov, A. Y., & Michaelis, I. (2017). Multi-MeV electron loss in the heart of the radiation belts. *Geophysical Research Letters*, *44*, 1204–1209. <https://doi.org/10.1002/2016GL072258>
- Shprits, Y. Y., Thorne, R. M., Friedel, R., Reeves, G. D., Fennell, J., Baker, D. N., & Kanekal, S. G. (2006). Outward radial diffusion driven by losses at magnetopause. *Journal of Geophysical Research*, *111*, A11214. <https://doi.org/10.1029/2006JA011657>

- Soraas, F., & Davis, L. R. (1968). temporal variations of the 100 keV to 1700 keV trapped protons observed on satellite explorer 26 during first half of 1965 (NO. N-68-34059; NASA-TM-X-63320; X-612-68-328). National Aeronautics and Space Administration, Greenbelt, Md. Goddard Space Flight Center.
- Summers, D., & Ma, C. Y. (2000). A model for generating relativistic electrons in the Earth's inner magnetosphere based on gyroresonant wave-particle interactions. *Journal of Geophysical Research*, *105*(A2), 2625–2639. <https://doi.org/10.1029/1999JA900444>
- Summers, D., Thorne, R. M., & Xiao, F. (1998). Relativistic theory of wave-particle resonant diffusion with application to electron acceleration in the magnetosphere. *Journal of Geophysical Research*, *103*(A9), 20,487–20,500. <https://doi.org/10.1029/98JA01740>
- Thorne, R. M., Li, W., Ni, B., Ma, Q., Bortnik, J., Chen, L., et al. (2013). Rapid local acceleration of relativistic radiation-belt electrons to efficient radiation belt electron acceleration: A superposed epoch analysis. *Geophysical Research Letters*, *42*, 6906–6915.
- Turner, D. L., Kilpua, E. K. J., Hietala, H., Claudepierre, S. G., O'Brien, T. P., Fennell, J. F., et al. (2019). The response of Earth's electron radiation belts to geomagnetic storms: Statistics from the Van Allen Probes era including effects from different storm drivers. *Journal of Geophysical Research: Space Physics*, *124*, 1013–1034. <https://doi.org/10.1029/2018JA026066>
- Turner, D. L., O'Brien, T. P., Fennell, J. F., Claudepierre, S. G., Blake, J. B., Jaynes, A. N., et al. (2016). Investigating the source of near-relativistic and relativistic electrons in Earth's inner radiation belt. *Journal of Geophysical Research: Space Physics*, *122*, 695–710. <https://doi.org/10.1002/2016JA023600>
- Turner, D. L., O'Brien, T. P., Fennell, J. F., Claudepierre, S. G., Blake, J. B., Kilpua, E. K. J., & Hietala, H. (2015). The effects of geomagnetic storms on electrons in Earth's radiation belts. *Geophysical Research Letters*, *42*, 9176–9184. <https://doi.org/10.1002/2015GL064747>
- Wanliss, J. A., & Showalter, K. M. (2006). High-resolution global storm index: Dst versus SYM-H. *Journal of Geophysical Research*, *111*, A02202. <https://doi.org/10.1029/2005JA011034>
- Wilken, B., Baker, D. N., Higbie, P. R., Fritz, T. A., Olson, W. P., & Pfizter, K. A. (1986). Magnetospheric configuration and energetic particle effects associated with a SSC: A case study of the CDAW-6 event on March 22, 1979. *Journal of Geophysical Research*, *91*(A2), 1459–1473. <https://doi.org/10.1029/JA091iA02p01459>
- Yuan, C. J., & Zong, Q.-G. (2012). Quantitative aspects of variations of 1.5–6.0 MeV electrons in the outer radiation belt during magnetic storms. *Journal of Geophysical Research*, *117*, A11208. <https://doi.org/10.1029/2011JA017346>
- Yuan, C., & Zong, Q. (2013). Relativistic electron fluxes dropout in the outer radiation belt under different solar wind conditions. *Journal of Geophysical Research: Space Physics*, *118*, 7545–7556. <https://doi.org/10.1002/2013JA019066>
- Yuan, C., & Zong, Q. G. (2019). The efficiency of Coronal Mass Ejection with different IMF preconditions on the production of MeV electron content in the outer radiation belt. *J. Geophys. Res. Space Physics*, *124*, <https://doi.org/10.1029/2018JA026263>
- Zhao, H., Baker, D. N., Jaynes, A. N., Li, X., Elkington, S. R., Kanekal, S. G., et al. (2017). On the relation between radiation belt electrons and solar wind parameters/geomagnetic indices: Dependence on the first adiabatic invariant and  $L^*$ . *Journal of Geophysical Research: Space Physics*, *122*, 1624–1642. <https://doi.org/10.1002/2016JA023658>
- Zhao, H., Baker, D. N., Li, X., Jaynes, A. N., & Kanekal, S. G. (2019). The effects of geomagnetic storms and solar wind conditions on the ultrarelativistic electron flux enhancements. *Journal of Geophysical Research: Space Physics*, *124*, 1948–1965. <https://doi.org/10.1029/2018JA026257>
- Zong, Q. G., Rankin, R., & Zhou, X. Z. (2017). The interaction of ultralow frequency Pc3 waves with charged particles in earth's magnetosphere. *Reviews of Modern Plasma Physics*, *1*(10). <https://doi.org/10.1007/s41614-017-0011-4>
- Zong, Q. G., Zhou, X. Z., Wang, Y. F., Li, X., Song, P., Baker, D. N., Fritz, T. A., Daly, P. W., Dunlop, M., & Pedersen, A. (2009). Energetic electron response to ULF waves induced by interplanetary shocks in the outer radiation belt. *Journal of Geophysical Research*, *114*, A10204. <https://doi.org/10.1029/2009JA014393>